Dynamic Characterization and Constitutive Modelling of ARMSTAL 500 Steel

Djalel Eddine TRIA[*], Radosław TRĘBIŃSKI

Department of Ballistics, Institute of Armament Technology,
Faculty of Mechatronics and Aerospace, Military University of Technology,
2 Sylwestra Kaliskiego St., 00-908 Warsaw, Poland
[*]*corresponding author, e-mail: dtria@wat.edu.pl, rkt@wat.edu.pl*

Abstract. The behaviour of a high strength steel (ARMSTAL 500) has been investigated using a combination of quasistatic and dynamic tests for a wide strain-rate range $1 \cdot 10^{-4} – 3 \cdot 10^{3}$ s^{-1}. A uniaxial testing machine and a Split Hopkinson Pressure Bar (SHPB) have been used under well controlled testing conditions. Next, the effect of the strain hardening, the strain rate hardening, loading history and stress triaxiality on the strength and ductility of the material has been studied. The present work also describes constitutive and damage models and their implementation available in the nonlinear finite element code LS DYNA. Calibration of constitutive model parameters and damage criteria is most often accomplished via regression techniques applied to laboratory data. A 3D numerical simulation of perforation of ARMSTAL 500 plates with 7.62×51 mm AP projectile were carried out with detailed models of target and compared with experiment in order to validate the calibrated models. As it will be shown, ARMSTAL 500 steel is a high strength steel with modest strain-rate sensitivity. The study indicates that the penetration depth can be predicted quantitatively and qualitatively with MJC hardening parameters calibrated from compression tests.

The Modified Johnson–Cook constitutive model with Cockcroft and Latham failure model can predict the projectile residual speed and the fragmentation process followed very closely by MJC failure criteria.

Keywords: Johnson–Cook strength model, damage models, Split Hopkinson Pressure bar, Material tests, LS DYNA Explicit

1. INTRODUCTION

In the design of protective structures, steel is still the dominating material although more advanced lightweight composites based armours are available [1-3]. Steels have high absolute strength and hardness combined with high ductility, low price compared to most other armour materials like composites and ceramics.

The computational studies in terminal ballistics require input data and improved material models. Since ARMSTAL 500 (30PM) is considered as low cost and interesting material due to its widespread usage in vehicle structure, there is no yet available material data required for describing its behaviour in the case of dynamic loadings.

In ballistic events, the modelling metallic materials are subjected to static and dynamic loads. The strain rates involved are $10^3 - 10^7$ s^{-1}, but it may be reduced to quasistatic values in the case of non-perforation. Therefore, the knowledge of exact model parameters over a wide range of strain rates is absolutely necessary.

There are a great number of constitutive equations available that have been proposed to describe the plastic behaviour of metallic materials as a function of strain hardening, strain- rate, and temperature. The objective is to collapse experimental data into one single equation. In this context, a useful model is the Johnson–Cook (JC) strength model [4, 5].

To meet the objectives of the study, a systematic combination of quasistatic tensile and compression tests with enhanced dynamic tests is presented which have allowed the determination of the ARMSTAL 500 steel properties in a strain rate range $1 \cdot 10^{-4} - 3 \cdot 10^3$ s^{-1}. A split Hopkinson pressure bar (Kolsky bar) has been used to determine the dynamic material properties under the impact compressive and tension loading conditions. This apparatus has become a commonly accepted test method for strain rates in the range of medium and high strain rates $10^2 - 10^4$ s^{-1} and has been used to test various engineering materials. The material property characterization experiments have been done under well-controlled testing conditions of the specimen in order for the experimental results to be clearly documented and interpreted.

A material description involves the stress-strain response as a function of large strains, high-strain rates, varying stress states, and history of loading. In addition to plastic flow at high strain, fracture is an important aspect of dynamic material characterization for engineering applications in structural impact.

However, a description of the accumulated damage and the mode of failure have been conducted.

In addition to this work, a numerical simulation of perforation of ARMSTAL 500 plates was carried out with detailed models *of* target and projectile, and compared with experiment in order to validate the calibrated models. A 3D explicit Lagrangian algorithm, including both elements and particles, is used in this study to automatically convert distorted elements into meshless particles during the course of the computation. As it will be shown, ARMSTAL 500 steel is a high strength steel with modest strain-rate sensitivity. The study indicates that the penetration depth can be predicted quantitatively and qualitatively with JC hardening parameters calibrated from compression tests. The Johnson–Cook constitutive model with Cockcroft and Latham failure model can predict the projectile residual speed and the fragmentation process followed very closely by JC failure criterion.

2. THE MATERIAL MODELS

2.1. The constitutive relation

A slightly modified version of the Johnson–Cook constitutive relation [4] is chosen for this study, based on traditional plasticity theory that reproduces several material responses observed in impact and penetration of metals. This computational model expresses the equivalent (von Mises) flow stress as a function of the equivalent plastic strain, strain rate, and temperature as [6, 9]

$$\sigma_{eq} = \left(A + B\varepsilon_{eq}^{n}\right)\left(1 + \dot{\varepsilon}_{eq}^{*}\right)^{C}\left(1 - T^{*m}\right) \tag{1}$$

where *A*, *B*, *C*, *n*, and *m* are the material constants, ε_{eq} is the effective plastic strain, $\dot{\varepsilon}_{eq}^{*}$ is the dimensionless plastic strain rate, $T^{*} = (T - T_{room})/(T_{melt} - T_{room})$ is the homologous temperature.

The first bracket in the model represents the strain hardening, the second describes the strain-rate sensitivity, and the third represents the temperature softening. This implies that the strain hardening, strain-rate hardening, and temperature softening are independent of each other, i.e. the different influences are uncoupled in this model. Thus, it is only necessary to perform material tests where these effects are studied separately in order to determine the material constants.

The rate of temperature increase is computed from the energy balance by assuming adiabatic conditions

$$\dot{T} = \chi \frac{\sigma_{eq}\,\dot{\varepsilon}_{eq}}{\rho\,c_p} \tag{2}$$

where ρ is the material density, c_p is the specific heat, and χ is the Taylor–Quinney coefficient that represents the proportion of plastic work converted into heat.

2.2. The fracture criteria

In many materials it is seen from experiments [5, 6] that failure strain increases with increasing temperature and may decrease with increasing strain rate, hence they both have an effect on the damage process during penetration. Johnson and Cook [5] made the failure strain ε_f dependent on strain path, strain rate and temperature, beside of being dependent on stress triaxiality. A slightly modified version of the original model, the MJC failure strain reads

$$\varepsilon_f = (D_1 + D_2 \exp(D_3\sigma^*))\left(1 + \dot{\varepsilon_{eq}}^*\right)^{D_4}(1 + D_5 T^*) \tag{3}$$

where $D_1 \ldots D_5$ are the material constants determined from material tests, $\sigma^* = \sigma_H/\sigma_{eq}$ is the stress triaxiality ratio where σ_H is the hydrostatic stress.

The fracture criterion was based on damage evolution, where the damage of a material element is expressed as:

$$\dot{D} = \begin{cases} 0 & for \quad \varepsilon_{eq} \leq \varepsilon_d \\ \\ \frac{D_c}{\varepsilon_f - \varepsilon_d}\dot{\varepsilon}_{eq} & for \quad \varepsilon_{eq} > \varepsilon_d \end{cases} \tag{4}$$

where D_c is the critical damage and ε_d is the damage threshold. The failure is assumed to occur when D equals unity.

Alternatively, damage failure can be modelled using a fracture criterion proposed by Cockcroft and Latham (CL) which was based on the total plastic work per unit volume expressed as follows [7]:

$$D = \frac{W}{W_{cr}} = \frac{1}{W_{cr}}\int_0^{\varepsilon_f}\langle\sigma_1\rangle \, d\varepsilon_{eq} \tag{5}$$

where W is the Cockcroft–Latham integral, σ_1 is the major principal stress, $<\sigma_1> = \sigma_1$ when $\sigma_1 \geq 0$ and $<\sigma_1> = 0$ when $\sigma_1 < 0$.

It is seen that fracture cannot occur in this model when there is no tensile stress operating, which implies that the effect of stress triaxiality on the failure strain is implicitly taken into account. Thus, W_{cr} remains fairly constant for varying temperature and strain rate.

The CL one-parameter fracture criterion is of special interest in design, since it requires only one simple tensile test in order to determine the material constant W_{cr}.

3. EXPERIMENTAL TESTS PROGRAM

3.1. Quasistatic tests

A high stability material testing machines MTS Criterion Model 45 and Instron 8862 were used to conduct various tensile and compression tests at five different strain rates $\dot{\varepsilon} = 10^{-4}$, 10^{-3}, 10^{-2}, 10^{-1}, 10^{0} sec^{-1} for the investigated ARMSTAL 500 steel, where the effects of strain hardening, strain rate and stress triaxiality on strength and ductility of the material were studied independently of each other. All the specimens are taken from 10-mm thickness plate using a wire electrical discharge machine. For each strain-rate, three specimens are tested.

For the quasistatic tensile tests, they have been performed at room temperature using both smooth and pre-notched axisymmetric specimens Fig. 1. Notched specimens with four different notched root radii were tested ($R = 0.5$ mm, 1 mm, 2 mm and 4 mm). The different notches introduce different levels of hydrostatic tension in the specimens during straining, which distinctly affect both the true stress and the strain to failure of the material. The initial radius of the gauge section was kept constant at $a = 3$ mm for all the specimens tested. During the tests, applied load, the diameter reduction of the necking area crosshead displacement and longitudinal strain were measured.

A 3D digital image correlation apparatus have been used to record the diameter reduction in the cross-sectional area of the specimen during straining until the fracture Fig. 2. For each test; the number of parallels was three. This gave total 15 tests for smooth specimens at five different strain rates, and total 12 tests for notched specimens with different curvature radii. The Cauchy stress and the logarithmic strain were calculated as:

$$\sigma = \frac{F}{A}, \qquad \varepsilon = 2 \cdot \ln\left(\frac{d_0}{d}\right) \tag{6}$$

where F is the applied load, A is the current cross-sectional area, d_0 and d represent the initial and current diameter of the specimen.

The experimental scatter among specimens of identical initial geometry was found negligible. Figure 3 gives the calculated Cauchy stress-logarithmic strain for both smooth and notched specimens based on the diameter reduction measurements. As it can be seen, the stress is increased and the fracture strain is reduced with decreasing curvature radius, i.e. increased level of hydrostatic tension in the material during straining.
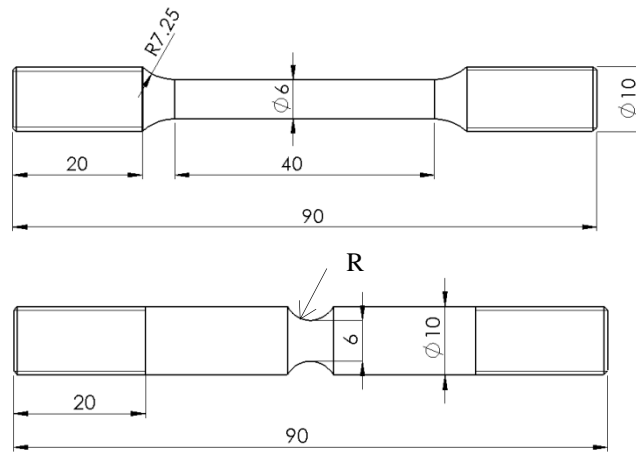
Fig. 1. Geometry and dimensions (in mm) of the smooth and pre-notched specimens used in tensile tests
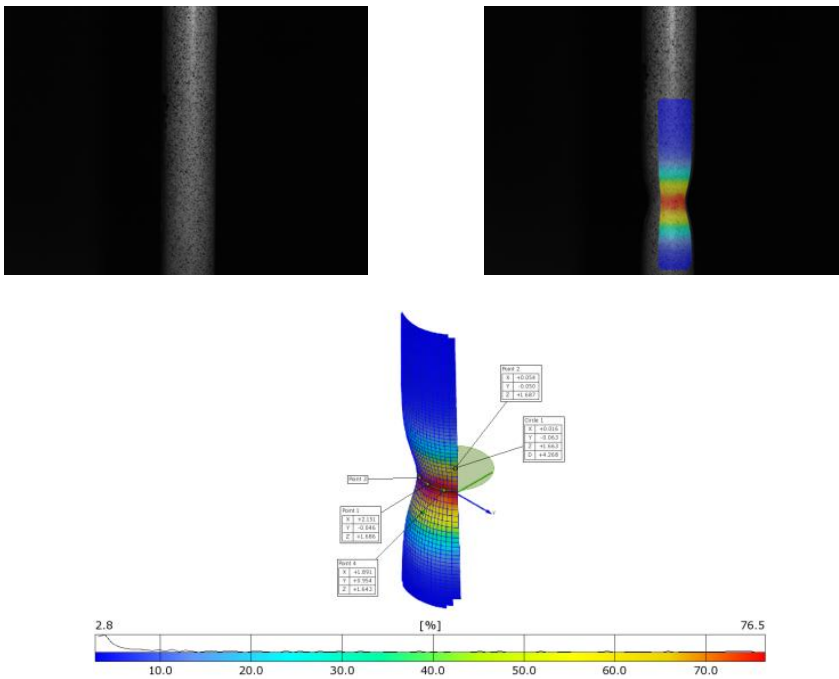

Fig. 2. Diameter reduction and major strain measurements over cross-section of necking area using 3D digital image correlation
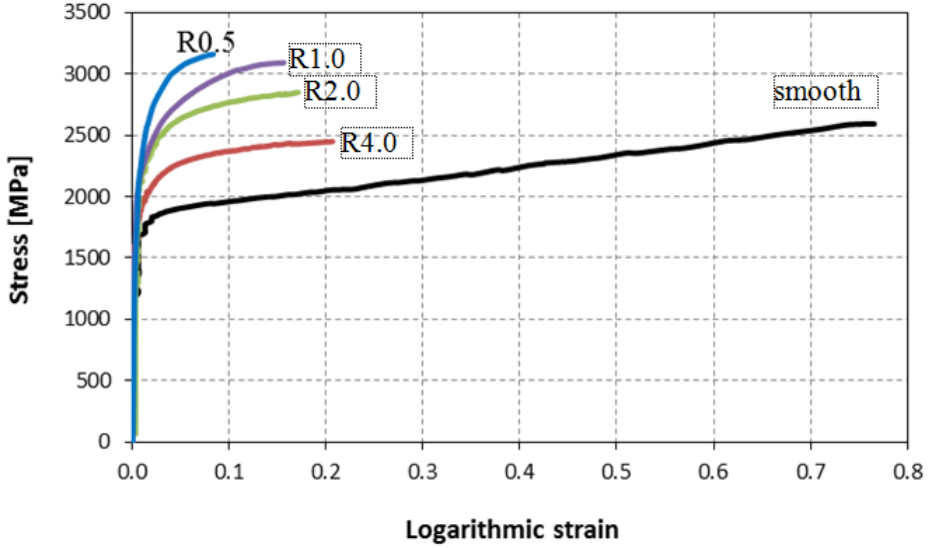
Fig. 3. Calculated Cauchy stress and logarithmic strain from quasistatic tensile tests on smooth and pre-notched specimens

The logarithmic plastic strain is obtained as $\varepsilon^p = \varepsilon - \sigma/E$, where E is the Young's modulus. Note that the measured Cauchy stress σ is equal to the major principle stress σ_1 in the uniaxial tension test. The true fracture strain was measured in all tests carried out. This parameter is given as

$$\varepsilon_f = \ln\left(\frac{A_0}{A_f}\right) \tag{7}$$

based on the original cross-section area A_0 and the final cross-section area A_f of the test specimen, and represents the maximum true strain the material withstands before fracture occurs.

For the quasistatic compression tests, the geometry of the specimens is shown in Fig. 4. The force F and the elongation are measured using a high precision load cell. The nominal stress and strain are determined according to $\sigma_s = F/A_s$ and $\varepsilon_s = \Delta L/L_s$, where A_s is the initial cross-sectional area of the specimen, ΔL is the shortening, and L_s is the initial length of the specimen. The true stress and true strains are calculated as,

$$\sigma_{true} = \sigma_s(1 - \varepsilon_s) \tag{8}$$

$$\varepsilon_{true} = -\ln(1 - \varepsilon_s) \tag{9}$$

The effective plastic strain is then obtained as

$$\varepsilon^p = \varepsilon_{true} - \sigma_{true}/E \tag{10}$$

where E is the Young's modulus.

Figure 5 represents the plot of true stress versus true strain at different strain rates.

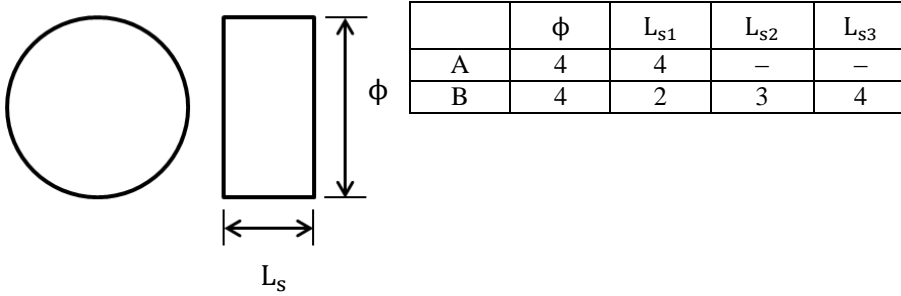|	ϕ	L_{s1}	L_{s2}	L_{s3}
A	4	4	–	–
B	4	2	3	4

Fig. 4. Geometry and dimensions of specimens used in a) quasistatic compression test,
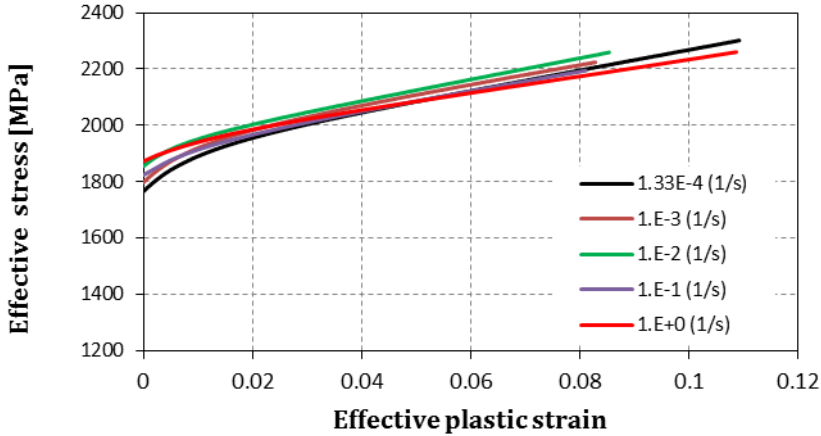b) dynamic compression tests

Fig. 5. Effective stress-strain curves from quasistatic compression tests at five
different strain rates

3.2. Dynamic tests

Compression tests for the higher strain rates (up to $\dot{\varepsilon} = 10^3$ s^{-1}) were conducted in a Split–Hopkinson bar. Load measurements were made with a strain gauge attached to elastic bars holding the specimen. The nominal stress, nominal strain, and nominal strain rate in the specimen are calculated with the following elastic relations

$$\sigma_s = \frac{A_B}{A_s} E_B \varepsilon_T \tag{11}$$

$$\varepsilon_s = \frac{-2C_B}{L_s} \int_0^t \varepsilon_R \, dt \tag{12}$$

$$\dot{\varepsilon}_S = -2\frac{C_B}{L_S}\varepsilon_R \qquad (13)$$

where A_B and A_s are the cross-sectional areas of the bars and the specimen, respectively; and E_B is the Young's modulus of the bar material, ε_R is the reflected strain history and ε_T is the transmitted strain history, C_B is the wave velocity in bars and L_s is the specimen length.

The average true stress, strain and strain rate in the specimen are calculated as Eq. (11, 12, and 13).
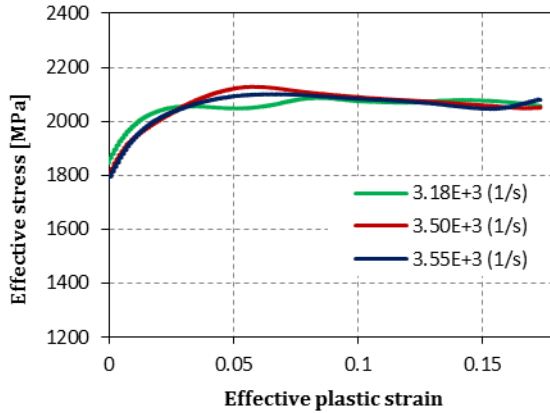
(a)
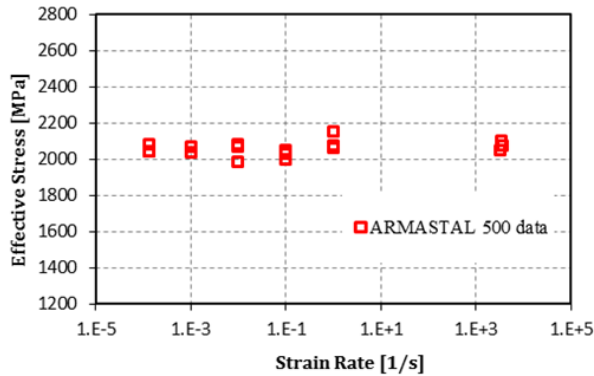
(b)

Fig. 6. (a) Calculated effective stress-strain curves from dynamic tests, (b) stress versus log strain-rate at 4% strain

Tensile tests for higher strain rates (up to $\dot{\varepsilon} = 10^3$ s^{-1}) were conducted in a modified Split–Hopkinson bar.
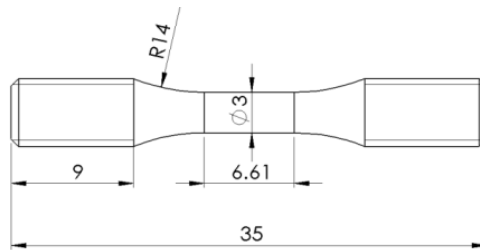
Fig. 7. Geometry and dimensions of the specimen for dynamic tensile tests

Here, the incident bar was clamped by a brittle bridge and pre-stressed in tension. When the bridge was broken, a uniaxial elastic tension wave propagated along the incident bar and loaded the specimen to fracture. Due to the numerous reflections of elasto-plastic waves in the short specimen, stress equilibrium was obtained. Strain gauges placed on the incident and output bar, at equal distances from the specimen, were used for measurements of the incident, reflected and transmitted pulses. The unfiltered data was used to calculate the nominal stress, strain, and strain-rate.

The experimental program consisted of 9 uniaxial compression tests in the strain rate range 3180-3550 s^{-1}, and the geometry of the specimen used in all tests is shown in Fig. 4. The number of parallels for each strain-rate tested was three, and the repeatability was found to be good. The true stress–strain curves at different strain-rates are shown in Fig. 6a. There is an insignificant difference between the three tested types of the specimens. Only three selected effective stress-strain curves are shown.

A decrease in the plastic stress flow has been noticed at high strain rates when the plastic strain increases. At plastic strain of 10%, the value of the stress obtained is 2082 MPa. This decrease is due to the thermal softening effect of the adiabatic heating. At high strain rates, the heat generated is accumulated in the sample due to the short duration time of the deformation.

Furthermore, the relationships between the log strain rates and the effective stresses estimated from the experimental results are shown in Fig. 6b. Each data point represents the effective stress at an effective plastic strain value of 4%. This assumption is used by Børvik et al. [3, 8] in which the strain rate is considered stable and without dynamic interference for all specimens. From Fig. 6b we can understand that PM 30 steel exhibits the modest strain-rate sensitivity due to the horizontal distribution of the effective stresses along the strain rate interval.

Unfortunately, it was not possible to use the modified Hopkinson bar with confidence at higher strain-rates for tensile tests.

4. IDENTIFICATION OF MATERIAL CONSTANTS

The basic idea of the identification procedure was to determine all material constants without the use of numerical simulations. This was found possible using a direct curve fit to the experimental data. The method of least squares requires the residual sum between the experimental observations and model results to be minimized.

The calibration of both, the modified JC constitutive relation and the modified JC failure criterion is presented in this paper, and it is based on extensive series of compression and tensile tests mentioned in the previous section. In the tests, the stress-strain relation and fracture strain were obtained for a wide range of strain-rates and stress triaxiality levels. Owing to the multiplicative form of the constitutive strain hardening, strain rate hardening, stress triaxiality could be calibrated separately. The temperature softening part is calibrated considering a linear relation between the plastic flow and temperature rise. This approach is extensively used for steel [3, 6].

To account for the increased stress triaxiality in the material after diffuse necking, the Cauchy stress was corrected for triaxiality effects using Bridgman's analysis to obtain the equivalent stress as

$$\sigma_{eq} = \frac{1}{3} + \ln\left(1 + \frac{a}{2R}\right) \tag{14}$$

where a is the initial radius of the specimen and R is the root radius of the notch. It is further assumed that the stress triaxiality is constant during straining, and that the plastic strain is constant over the cross-section of the neck. Figure 8 shows the experimental data for both tensile and compression tests that were used in the calibration of the modified JC constitutive relation, the modified JC failure criteria and Cockcroft and Latham failure criterion. The material constants for the modified JC constitutive relation and failure criteria for ARMSTAL 500 steel are given in Tables 1 and 2.

Figure 9 represents the calculated stress-strain curves at 10^{-4} for ARMSTAL steel and its equivalent grades. As it is shown, the described steel has almost the same strain hardening slopes, and the studied steel is very similar to ARMOX 500T.

(a)

(b)

(c)
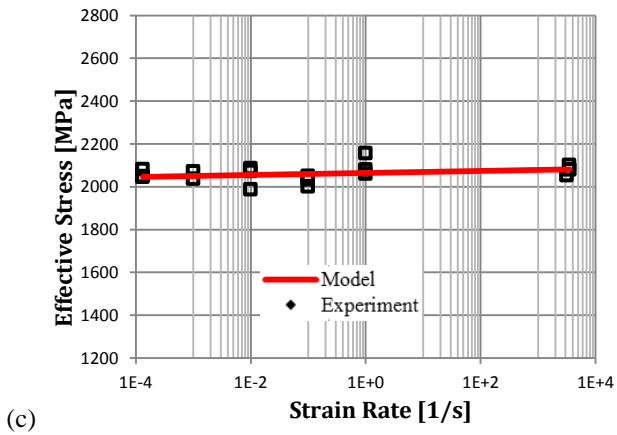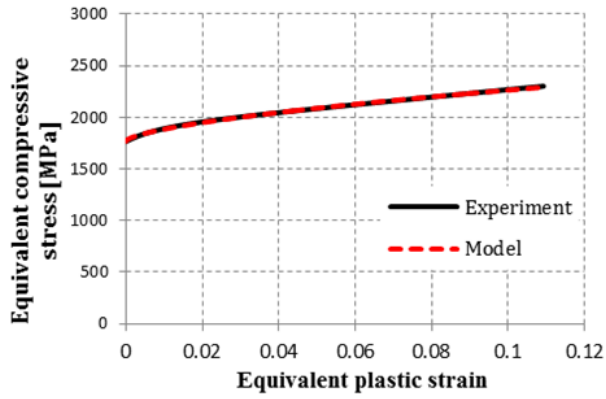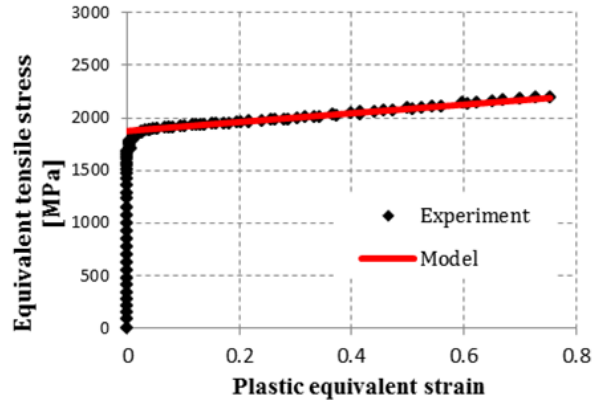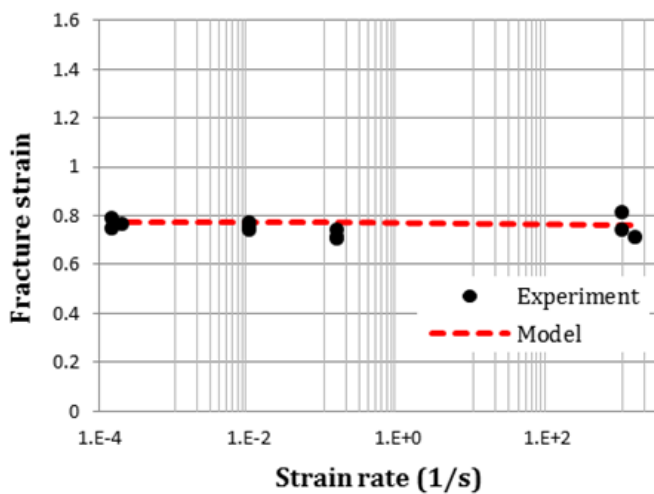
(d)
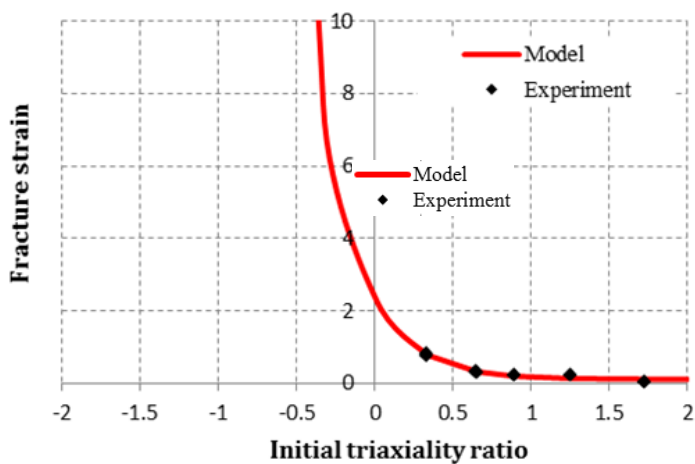
(e)

Fig. 8. Comparison between experimental data and model results
for ARMSTAL 500 steel

Table 1. Hardening constants for ARMSTAL 500 steel and their equivalent grades.

| Material	Hardness	Yield stress	Strain hardening			Strain rate hardening		Temperature softening
	HB	$\sigma_{0.2}$ MPa	A MPa	B MPa	n	C	$\dot{\varepsilon}_0$ (s^{-1})	m
ARMSTAL 500	488-566	1707	1875	415	0.98	0.0010	$2 \cdot 10^{-4}$	1.0
Domex Protect 500 [2]	477-550	1592	2030	504	1.0	0.0010	$5 \cdot 10^{-4}$	1.0
Armox 560T [2]	530-590	1711	2030	568	1.0	0.0010	$5 \cdot 10^{-4}$	1.0
Armox 500T [3]	480-540	1250	1470	702	0.199	0.0054	$5 \cdot 10^{-4}$	1.0
Secure 500 [3]	480-530	1300	1299	2230	0.5585	0.04447	$5 \cdot 10^{-4}$	0.961
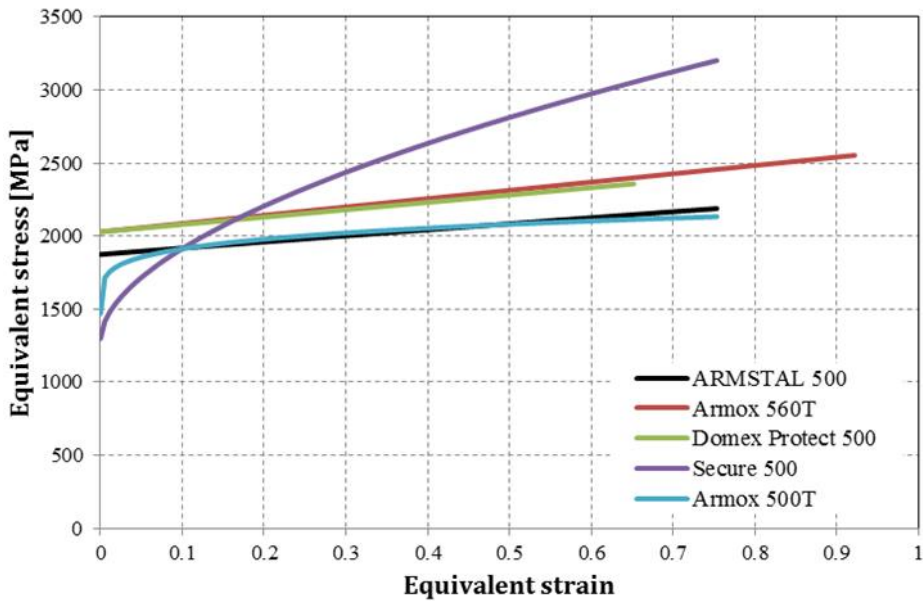
Fig. 9. Calculated stress-strain curves at 10^{-4} for ARMSTAL 500 steel and its equivalent grades

Table 2. Material parameters for the fracture criteria obtained for the ARMSTAL 500 steel plates

Material	Modified Johnson–Cook (MJC)					Cockcroft −Latham (CL)	Maximum shear stress	Constant failure strain
	D_1	D_2	D_3	D_4	D_5	W_{cr} (MPa)	τ_{max} (MPa)	ε_f
30PM	0.1088	2.281	-3.649	-0.0012	0	1689	1546	0.752

5. VALIDATION OF THE CONSTITUTIVE MODEL AND FAILURE CRITERIA

In order to validate the calibrated models described in the previous section, a 3D numerical simulation of perforation of ARMSTAL 500 plates with Stanag 4569 level 3 7.62 × 51 mm AP ammunition were carried out using the explicit Finite Element code LS-DYNA [9, 10]. An exemplary of the geometric model is shown in Fig. 10.
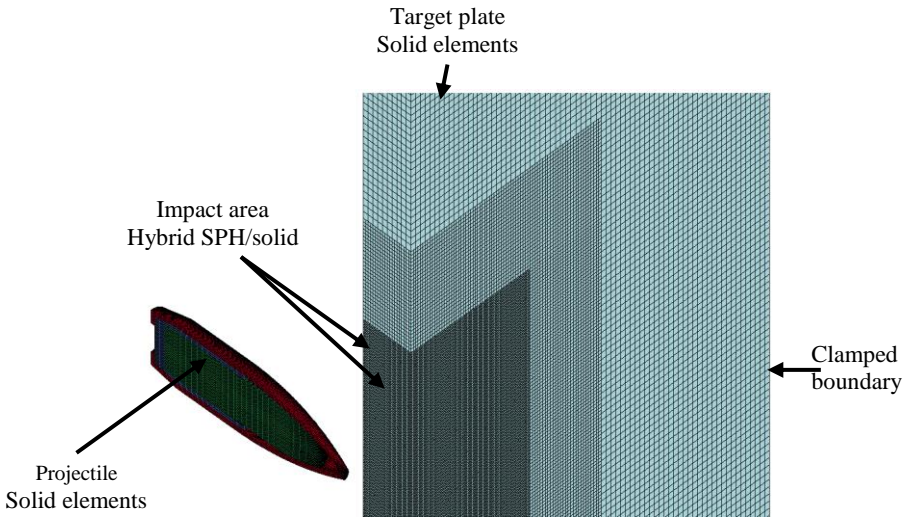

Fig. 10. Plot of a typical initial mesh for the fine model (7.62 mm AP bullet; ARMSTAL 500 steel plate). The model has been cut in half to show the interior

The bullet ammunition consists of a hardened steel core N12E, brass jacket, and a lead sabot. Note that material parameters for bullet different parts have been taken from literature [11]. The target plate is divided into three mesh regions. The mesh is coursing from the impact area to the outer edge of the plate. The model is meshed with hexahedral constant stress solid elements of varying size between 0.2 and 0.8 mm.

Exception for the plate impact area which subjected to large deformation and elements erosion, hybrid SPH/solid elements have been used. This approach allows the conversion of the eroded solid elements to Smooth Particles Hydrodynamics. The generated particles keep the same mechanical properties and mass of the eroded elements. Ballistic tests have been performed at the Laboratory of Ballistics of the Military University of Technology. The obtained experimental data have been used for the comparison with numerical simulations. A serial of normal impact and perforation of steel plates with different selected thickness: 2×8 mm, 8 mm, 6 mm, 3 mm subjected to 7.62×51 mm AP bullet at the initial velocity of 835 m/s.

Table 3. General material constants for the MJC constitutive relation

Material	E (MPa)	v	ρ (kg/m^3)	c_p (J/kgK)	χ	α (K^{-1})	T_c^*
All steel alloys	210,000	0.33	7850	452	0.9	$1.2 \cdot 10^{-5}$	0.9
Lead sabot	1000	0.42	10,660	124	0.9	$2.9 \cdot 10^{-5}$	0.9
Brass jacket	115,000	0.31	8520	385	0.9	$1.9 \cdot 10^{-5}$	0.9

Table 4. Bullet material constants for the MJC relation

Material	Strain hardening			Strain rate hardening		Temperature softening		
	A (MPa)	B (MPa)	n	C	$\dot{\varepsilon}_0$ (s^{-1})	T_r (K)	T_m (K)	m
N12E Core	1200	50,000	1.0	0	$5 \cdot 10^{-4}$	293	1800	1.0
Lead sabot	24	300	1.0	0.1	$5 \cdot 10^{-4}$	293	760	1.0
Brass jacket	206	505	0.42	0.01	$5 \cdot 10^{-4}$	293	1189	1.68

Figures 11 and 12 represent the results of penetration of 8 mm plate and 2×8 mm plates. It is clear that the modified Johnson–Cook model calibrated from tensile tests has overestimated the penetration depth. However, the model calibrated from compression tests gives a good agreement with experimental results. This is due to the effect of strain hardening of the material which considered important in case of compression more than in tension loading.
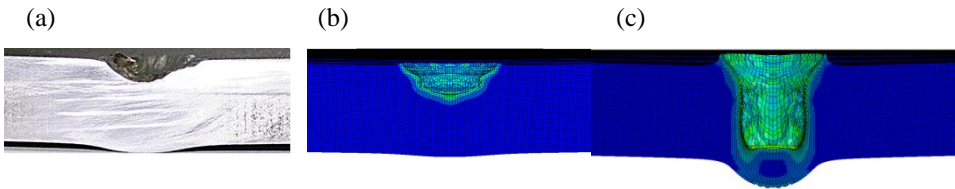
Fig. 11. A comparison between experimental crater shape of 8 mm plate (a) and modified Johnson–Cook model prediction; (b) material parameters determined from compressive tests; (c) material parameters determined from tensile tests
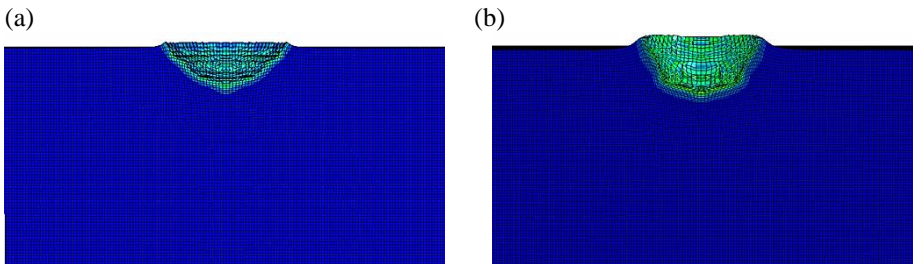

Fig. 12. A comparison between experimental crater shape of 2 × 8 mm plate (a) and modified Johnson–Cook model prediction; (a) material parameters determined from compressive tests; (b) material parameters determined from tensile tests

High-speed camera images of a perforation test on 3 mm and 6 mm thickness ARMSTAL 500 target were compared with the numerical results at identical impact velocity using numerical models described above. Results from numerical simulations showed the physical behaviour of the structure have been well described for all used models (Fig.13, 14) for both plate thicknesses. Thus, the predicted projectile residual speed was in the range of the obtained experimental data (Fig. 15, 16).
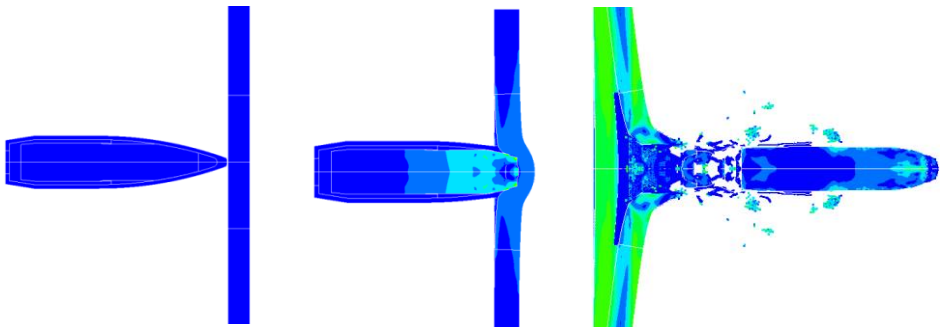

Fig.13. Some plots from numerical simulations showing a 7.62-mm ball bullet during impact of the 3 mm ARMSTAL 500 steel plate
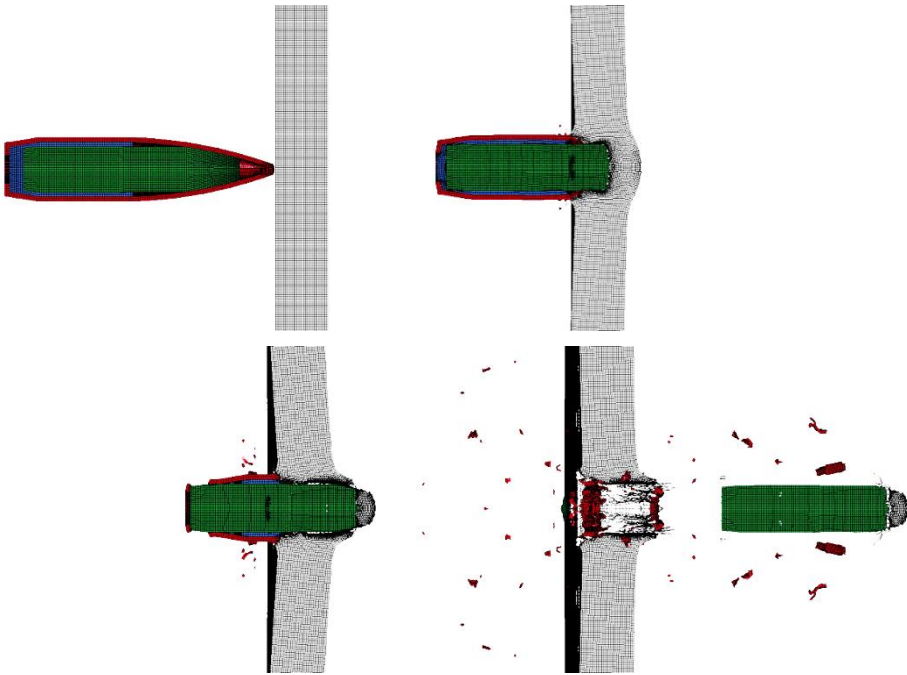
D.E. Tria, R. Trębiński

Fig. 14. Some plots from numerical simulations showing a 7.62-mm ball bullet during
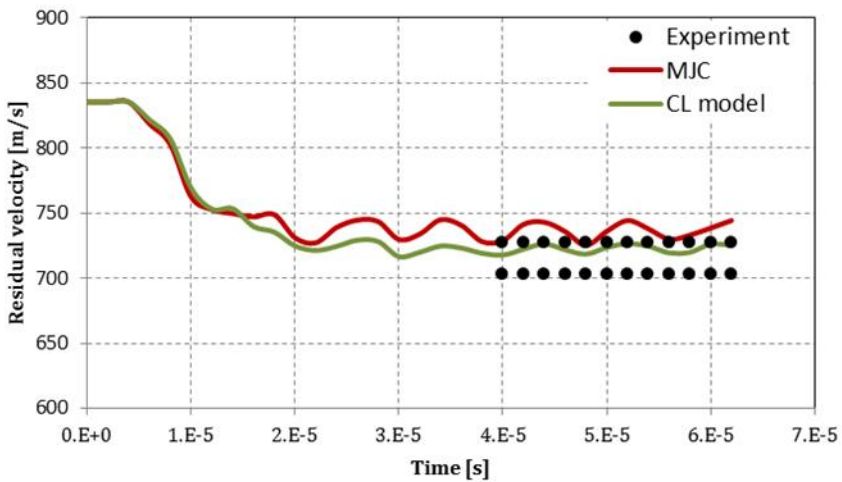impact of the 6 mm ARMSTAL 500 plate

Fig. 15. Comparison between experimental and numerical projectile residual velocity
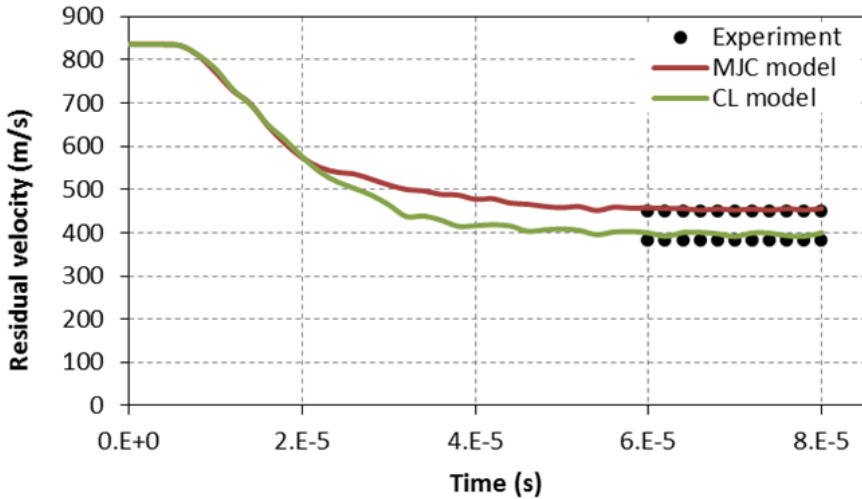after penetrating 3 mm plate

Fig.16. Comparison between experimental and numerical projectile residual velocity after penetrating 6 mm plate

6. CONCLUDING REMARKS

In this study, a systematic combination of quasistatic standard compression and tensile tests with enhanced dynamic tests is presented which have allowed the determination of the ARMSTAL 500 steel behaviour in a strain rate range $1 \cdot 10^{-4} - 3 \cdot 10^3$ s^{-1}. The effect of the strain hardening, the strain rate hardening, loading history and stress triaxiality on the strength and ductility of the material has been studied. A 3D numerical simulation of perforation of ARMSTAL 500 plates with 7.62 × 51 mm AP projectile were carried out with detailed models of target and compared with experiment in order to validate the calibrated models. According to numerical and experimental data developed during the study, the following main conclusions can be drawn:

- The studied ARMSTAL 500 steel showed a high strength with modest strain-rate sensitivity. The Modified Johnson–Cook material model derived for target material is capable to characterize the deformation behaviour during penetration.
- The material model has similar parameters when compared with the available literature based data for steel which has the hardness around 500 HB.
- The study indicates that the penetration depth can be predicted quantitatively and qualitatively with MJC hardening parameters calibrated from compression tests.

- The Modified Johnson–Cook constitutive model with Cockcroft and Latham failure model can predict the projectile residual speed and the fragmentation process with a good agreement to the experimental observations. The reason why the modified Johnson–Cook failure model has overestimated the projectile residual speed is that model parameters have been calibrated considering the stress triaxiality ratio remains constant during tensile loading.
- This study showed also that the 3D Finite Elements algorithm with Hybrid approach is capable to predict the armour steel plate deformation and failure behaviour when it is subjected to armour piercing projectile at high velocity impact.

Acknowledgements

REFERENCES

[1] Cheeseman B.A., Bogetti T.A., Ballistic impact into fabric and compliant composite laminates, *Composite Structures*, vol. 61, pp. 161-173, 2003.

[2] Gama B.A., Bogetti T.A., Fink B.K., Yu C.J., Claar T.D., Eifert H.H., et al., Aluminum foam integral armour: a new dimension in armour design, *Composite Structures*, vol. 52, pp. 381-395, 2001.

[3] Børvik T., Dey S., Clausen A.H., Perforation resistance of five different high-strength steel plates subjected to small-arms projectiles, *International Journal of Impact Engineering*, vol. 36, pp. 948-964, 2009.

[4] Johnson G.R., Cook W.H., A Constitutive model and data for metals subjected to large strains, high strain rates and high temperatures, *Proceedings of the 7th International Symposium on Ballistics*, The Hague, The Netherlands, April 1983.

[5] Johnson G.R., Cook W.H., Fracture characteristics of three metals subjected to various strains, strain rates, temperatures and pressures, *Engineering Fracture Mechanics*, vol. 21, pp. 31-48, 1985.

[6] Hancock J.W., Meckenzie, A.C., On the mechanisms of ductile failure in high strength steels subjected to multi-axial stress-states, *Journal of the Mechanics and Physics of Solids*, vol. 24, pp. 147-169, 1976.

[7] Cockcroft M.G., Latham D.J., Ductility and the workability of metals, *Journal of the Institute of Metals*, vol. 96, pp. 33–39, 1968.

[8] Børvik T., Hopperstad O.S., Berstad T., Langseth M., A computational model of viscoplasticity and ductile damage for impact and penetration, *European Journal of Mechanics – A/Solids*, vol. 20, pp. 685-712, 2001.

[9] Hallquist J. O., *LS-DYNA. Keyword User's Manual*, V971 R6.1.0, LSTC Co., CA, USA 2009.

[10] Zukas J.A., *Introduction to Hydrocodes*, Computational Mechanics Associates, Baltimore, 2004.

[11] Børvik T., Olovsson L., Dey S., Langseth M., Normal and oblique impact of small arms bullets on AA6082-T4 aluminium protective plates, *International Journal of Impact Engineering*, vol. 38, pp. 577-589, 2011.